Writing SAMs with Cs: optimization of atomic nanolithography imaging using self-assembled monolayers on gold substrates

C. O'Dwyer,* G. Gay, B. Viaris de Lesegno,† and J. Weiner

Institut de Recherche sur les Systèmes Atomiques et Moléculaires Complexes,

Laboratoire de Collisions, Agrégats et Réactivité,

UMR CNRS 5589, Université Paul Sabatier,

118 route de Narbonne, 31062 Toulouse Cedex 4, France

K. Ludolph, D. Albert,‡ and E. Oesterschulze‡

Institute of Microstructure Technology and Analytics,

University of Kassel, 34132 Kassel,Germany

(Dated: December 16, 2004)

Abstract

We report the results of a study into the factors controlling the quality of nanolithographic imaging. Self-assembled monolayer (SAM) coverage, subsequent post-etch pattern definition and minimum feature size all depend on the quality of the Au substrate used in material mask atomic nanolithographic experiments. We find *sputtered* Au substrates yield much smoother surfaces and a higher density of {111} oriented grains than *evaporated* Au surfaces. Phase imaging with an atomic force microscope (AFM) shows that the quality and percentage coverage of SAM adsorption is much greater for sputtered Au surfaces. Exposure of the SAM to an optically-cooled atomic Cs beam traversing a two-dimensional array of submicron material masks mounted a few microns above the SAM surface allowed determination of the minimum average Cs dose (2 Cs atoms per SAM molecule) to write the monolayer. Suitable wet-etching, with etch rates of 2.2 nm min^{-1}, results in optimized pattern definition. Utilizing these optimizations, material mask features as small as 230 nm in diameter with a fractional depth gradient of 0.8/20 nm were realized.

PACS numbers: 32.80.Pj, 39.25.+k, 61.10.Nz, 68.37.Ps, 68.55.Jk, 81.07.-b, 81.16.Ta

*Present address: Photonic Nanostructures Group, Tyndall National Institute, Cork, Ireland

†Present address: Laboratoire Aimé Cotton, Campus d'Orsay, 91405 Orsay, France

‡Present address: Technische Universität Kaiserslautern, 67663 Kaiserslautern, Germany

I. INTRODUCTION

Over the last ten years, considerable research efforts have been devoted to developing processes for nanoscale feature definition below the diffraction limit. The pioneering work performed by Timp *et al.* [1, 2] and McClelland *et al.* [3] used a method for nanostructure fabrication based on a standing optical wave to focus neutral atoms. The method does not use a material mask or resist, but relies on optical forces to focus a flux of atoms on solid substrates. Since the atomic de Broglie wavelength is of sub-nanometer order at conventional atomic beam temperatures, the structure size was not subject to matter wave diffraction limitations. McClelland deposited lines of Cr as narrow as 38 nm full width at half maximum, spaced by 213 nm. These early studies stimulated several variants in the field of neutral atom nanolithography using optical masks [3–5] and material masks [6, 9].

Many of the atoms that are easily manipulated with atom optics are either highly reactive or volatile, so that they are not suitable for the creation of durable, permanent structures using direct deposition; consequently, the development of patterned chemical resist methods that are sensitive to alkali and other neutral atoms is worthwhile exploring.

A. Resist-based atomic nanolithography

Utilizing resists in neutral atom nanolithography provides both a high sensitivity to neutral atoms and a high resolution [7]. These resists can be categorized into two classes: self-assembled monolayers (SAMs) of organic molecules, and materials deposited onto a surface from a background vapor [8]. Berggren and co-workers [9] have demonstrated the modification of the chemical properties of a thin film made from a self-assembled monolayer (SAM) of organic molecules on a surface. They used a beam of metastable argon atoms patterned by a material mask instead of a light mask as described above.

Lithography at nanometer scales (< 100 nm) requires resists thin enough that they yield features with reasonable aspect ratios between the horizontal and vertical dimensions. The use of self-assembled monolayers (SAMs) as suitable resists has been the subject of much recent research because they furnish a uniform, organic, reactive surface and as a consequence, are thought to be technologically important [10–15]. Among the many SAM systems that have been investigated, those made by adsorbing alkanethiols on single-crystal

gold surfaces have been most frequently studied because of their ease of preparation and excellent stability [16]. SAMs have particular advantages for the fabrication of nanometer scale features relative to polymeric resists. The molecular diameter of the species in the SAM is small (<1 nm) and the corresponding films formed are sufficiently thin that they minimize scattering of incident particles or atoms within the film [8, 17]. However, one major disadvantage is the lack of knowledge surrounding the reactive mechanism of the SAM when exposed to a flux of alkali atoms, Cs for example. To generate useful contrast to chemical etchants between exposed and unexposed regions, a sufficient dose of atoms must be provided, but it must not over-expose to outlying regions. Furthermore, the structure formation is strongly affected by migration, agglomeration and local interaction of the atoms deposited on the surface. Although the explicit behaviour of such properties has not yet been widely investigated, details of the atom−surface interaction certainly plays a crucial role in atomic nanolithography experiments.

B. Alkanethiol self-assembled monolayers on Au

The principal ingredient for obtaining self-assembly is a relatively strong interfacial binding asymmetry of the molecular constituents. In the alkanethiol SAM case, this asymmetry is provided by the sulfur affinity for gold, and a comparably strong lateral interaction (4−8 kJ mol^{-1} per CH_2) [18], arising from the van der Waals forces between the alkyl chains that compose the backbone of each alkanethiol molecule. This lateral interaction can be controlled by changing the length of the hydrocarbon. While the lateral interactions are well characterized, the sulfur-gold binding in the alkanethiol-gold SAMs has remained the subject of frequent debate [19]. This is especially true in neutral Cs atomic nanolithography experiments where alkanethiol SAMs are utilized as positive resists. The modification of the SAM on exposure, which is believed to stem from the Cs attack on the Au−S bond, allows replication of a lithographic material mask down to submicron dimensions. Such spatial resolution is possible due to the high density molecular coverage ($\simeq 4 \times 10^{14}$ cm^{-2}) which corresponds to an small minimum molecular unit area of 4 nm^2. Site-specific changes in the affinity of the SAM to the gold surface can be probed by lateral force microscopy that can measure adhesion forces of the molecules to the surface.

Recently, the feature sizes of patterns written into SAMs through techniques such as

scanning near field photolithography (SNP) [20, 21], dip-pen nanolithography [22] and microcontact printing [23, 24] have been shown to be limited by the morphology of the granular metal surface which has represented a resolution limit for metal-substrate-based lithography. This resolution issue was addressed by Love *et al.* [25] who reported that Pd substrates yielded better post-etch resolution than their Au counterparts when coated with alkanethiol monolayers for nanolithographic purposes. We have recently reported [26] that a resolution limit of $\simeq 20$ nm is found when 1-nonanethiol SAMs are adsorbed on sputtered Au substrates. The results indicated that the quality of the Au surface is paramount in realizing a low defect-density molecular monolayer.

In this paper, we present the results of a study into the dependency of SAM coverage, subsequent post-etch pattern definition and minimum feature size on the quality of the Au substrate used in both material mask and optical mask atomic nanolithographic experiments. In particular, this paper addresses the essential properties required for optimization and reliable performance of submicron SAM patterning on Au substrates by wet-etching techniques. Such information is derived from studies of the quality of the monolayer coverage and optimization of the etching mechanism. In Sections III A and III B we present a detailed study of the sputtered Au substrates. We then outline and discuss our findings on the structure, uniformity and substrate dependent factors affecting the coverage by the SAM layer, using lateral force microscopy (LFM) in Section III C. In Section III D we present analysis of the dependency of 1-nonanethiol exposure on the Cs atom dose and a study of the etch rate of Au covered with exposed SAM molecules, so as to maximize etch pattern definition. Finally in Section III E we present observations of submicron features patterned into 1-nonanethiol on sputtered Au substrates, using material lithographic masks.

II. EXPERIMENTAL

The Si(100) substrates were loaded, as received, into the sputtering chamber. A 4 nm thick Cr adhesion layer was sputtered for 6 s at 1000 W and subsequently a 30 nm thick Au layer was sputtered for 60 s at 300 W. Both were sputtered at a base pressure of 8 $\times$ 10^{-6} Pa. Substrates coated in this manner are hereafter designated Au:1. A 4 nm thick Cr layer and a 30 nm thick Au layer were also coated onto Si substrates by thermal evaporation under similar conditions. These substrates are designated Au:2. Prior to any

treatment, both types of Au surfaces were cleaned in ethanol and immersed in a 3:1 mixture of H_2SO_4:H_2O_2 at 398 K for 5 minutes to remove any organic contaminants. After rinsing with deionized water, the Au samples were immediately placed in a 10^{-3} mol dm^{-3} solution of 1-nonanethiol $CH_3(CH_3)_8SH$ (95%, Aldrich) in reagent grade ethanol and then incubated at room temperature for over 24 h. In the 24 h period, a self-assembled monolayer of thickness $\simeq 1$ nm formed. After incubation, samples were rinsed with ethanol and examined microscopically. All samples were exposed to the Cs flux using an atomic beam flux as detailed in Section III E. Etching of exposed samples was carried out using a water-based etching solution composed of 1 mol dm^{-3} KOH, 0.1 mol dm^{-3} $K_2S_2O_3$, 0.01 mol dm^{-3} $K_3Fe(CN)_6$ and 0.001 mol dm^{-3} $K_4Fe(CN)_6$.

The crystallinity characterization was carried out by grazing incidence X-ray diffraction (GIXRD) [28] with a step width of 0.01°, using a Philips PW-1710 diffractometer with a Cu anode (radiation K_α of $\lambda = 1.54186$ Å).

X-ray rocking curves were performed on a Rigaku X-ray diffractometer with CuK_α radiation and were acquired by fixing the 2θ angle to that of the Au{111} reflection. X-ray rocking curves were acquired of the substrate and Cr layer in order to obtain the physical rocking curve of the Au overlayer by subtraction and deconvolution of all spectra.

All atomic force microscopy (AFM) and scanning tunnelling microscopy (STM) examinations were performed in ambient laboratory conditions (pressure and temperature). AFM and STM characterization was performed with a PicoSPM (Molecular Imaging, Inc.) and a Nano-R AFM (Pacific Nanotechnologies, Inc.). The STM tips were mechanically cut from 250 μm Pt/Ir (80:20) wire, electrochemically etched, polished, and tested on highly ordered pyrolytic graphite. Unless otherwise stated, the STM images were acquired at a bias voltage of +1.50 V in constant height mode. Images were acquired with high gap impedances to maximize the contribution from the alkanethiol monolayer [29, 30], and in particular, gap impedances of $\simeq 7-10$ GΩ [31] were required to resolve individual atoms. Atomic resolution STM images of monatomic steps in a Au{111} single crystal, evaporated on mica and flame annealed was conducted in order to calibrate the vertical height. Atomically resolved STM of the Au surface used in the experiments was also conducted to determine the crystallographic orientation of the sample with respect to the STM scan direction. Atomic resolution and topological AFM imaging was performed in both contact and AC tapping modes. Topological information was supplemented by lateral force and phase modulation

imaging respectively to determine adhesion force changes and composition differences in the surfaces examined. Soft Si_3N_4 tipped cantilevers with a spring constant of 0.12 nN nm^{-1} were used in contact mode. Comparisons were made with STM images to examine whether any tip-induced reconstruction of the monolayer took place during imaging under STM.

III. RESULTS AND DISCUSSION

A. Comparison of sputtered and evaporated Au surfaces

Non-contact tapping mode AFM was employed to characterize the topography of both the Au:1 and Au:2 surfaces. Figures 1a and 1b show the surface topography of the Au:1 and Au:2 surfaces respectively. It can be observed that the Au:2 surface is much rougher than that of the Au:1 surface and contains a well pronounced grain structure. The *rms* roughness of the Au:1 and Au:2 surfaces was determined from the AFM data in Figs. 1a and 1b and is measured to be 1.8 ± 0.4 nm and 6.7 ± 1.2 nm respectively. Such smooth Au:1 surfaces are formed by sputtering at low power, which was necessary to produce a smooth surface over a granular 4 nm thick Cr adhesion layer. This smoothness is highlighted more clearly in the magnified image of the surface in Fig. 1c. In Fig. 1d, which is a magnified AFM image of the highly granular Au:2 surface shown in Fig. 1b, the undulating grain structure is clearly observed.

High resolution AFM imaging of the Au:1 surface was also conducted to characterize the surface morphology and growth mechanism of the very smooth grains observed. This imaging technique was not possible, however, for the highly undulating rough Au:2 surface. Figure 2 shows a 200×200 nm AFM image of the Au:1 surface in height-mapped grayscale. A line scan through the "terraced" area of the surface, indicated on the image, is shown in Fig. 2b. It is observed that the height difference between each of the Au terrace layers is approximately 0.25 nm, almost equivalent to the Au monatomic step height (0.2355 nm), indicating that Au monolayers (defined in the images by the terraces within the grain) are atomically flat and thus single crystal. Highlighted in the image are examples of individual monatomic depressions of the Au surface. Such depressions are noted to be present over the whole surface prior to SAM adsorption and we have recently shown that these pits can increase the defect density of any organic monolayer adsorbed on the surface [26].

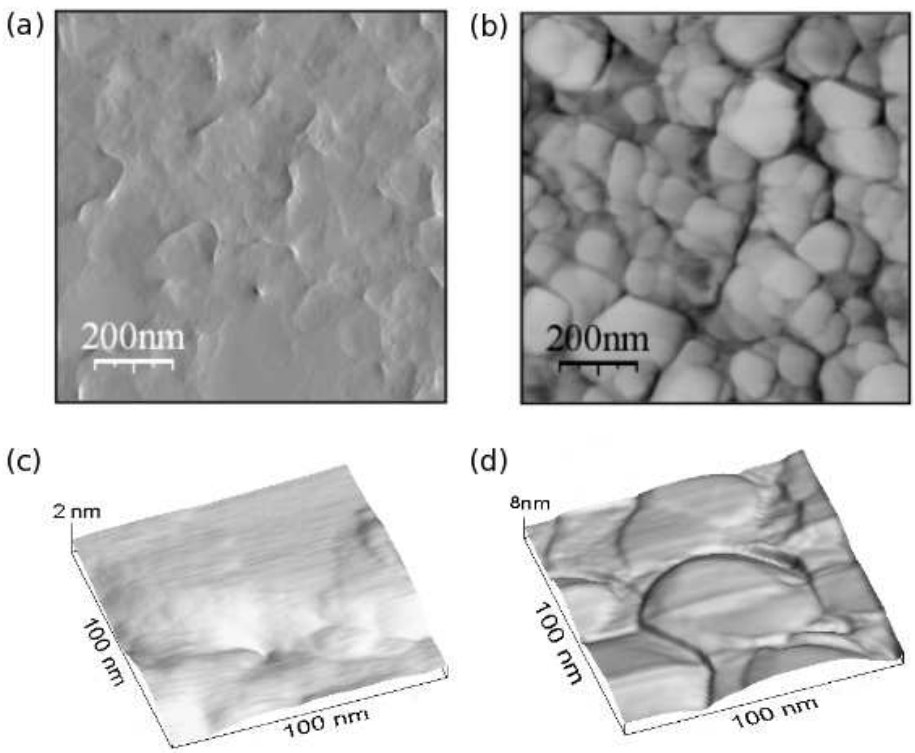

FIG. 1: (a) 1 μm $\times$ 1 μm tapping mode survey AFM image of the sputtered Au:1 surface immediately prior to immersion in the alkanethiol bath solution. (b) 1 μm $\times$ 1 μm tapping mode AFM image of the evaporated Au:2 surface under the same imaging conditions. (c) 100 nm $\times$ 100 nm higher magnification image of the Au:1 surface showing a smooth surface with a segment of a large grain visible. (d) 100 nm $\times$ 100 nm higher magnification AFM image of the rougher Au:2 surface where multiple grains can be seen.

B. Comparison of the physical properties of sputtered and evaporated Au substrates

1. Grain size

Constant current STM images were acquired of various regions of both the Au:1 and Au:2 surfaces under ambient conditions in air to determine the average grain size. Images were obtained at sample bias between 50 and 200 mV and tunnelling current between 1 and 2 nA. STM images of the Au:1 and Au:2 surfaces are shown in Figs. 3a and 3b, where individual grains are resolved. We employed fractal analysis [32] to analyze the grain structure responsible for the surface roughness observed in the STM topographies and used a suitable

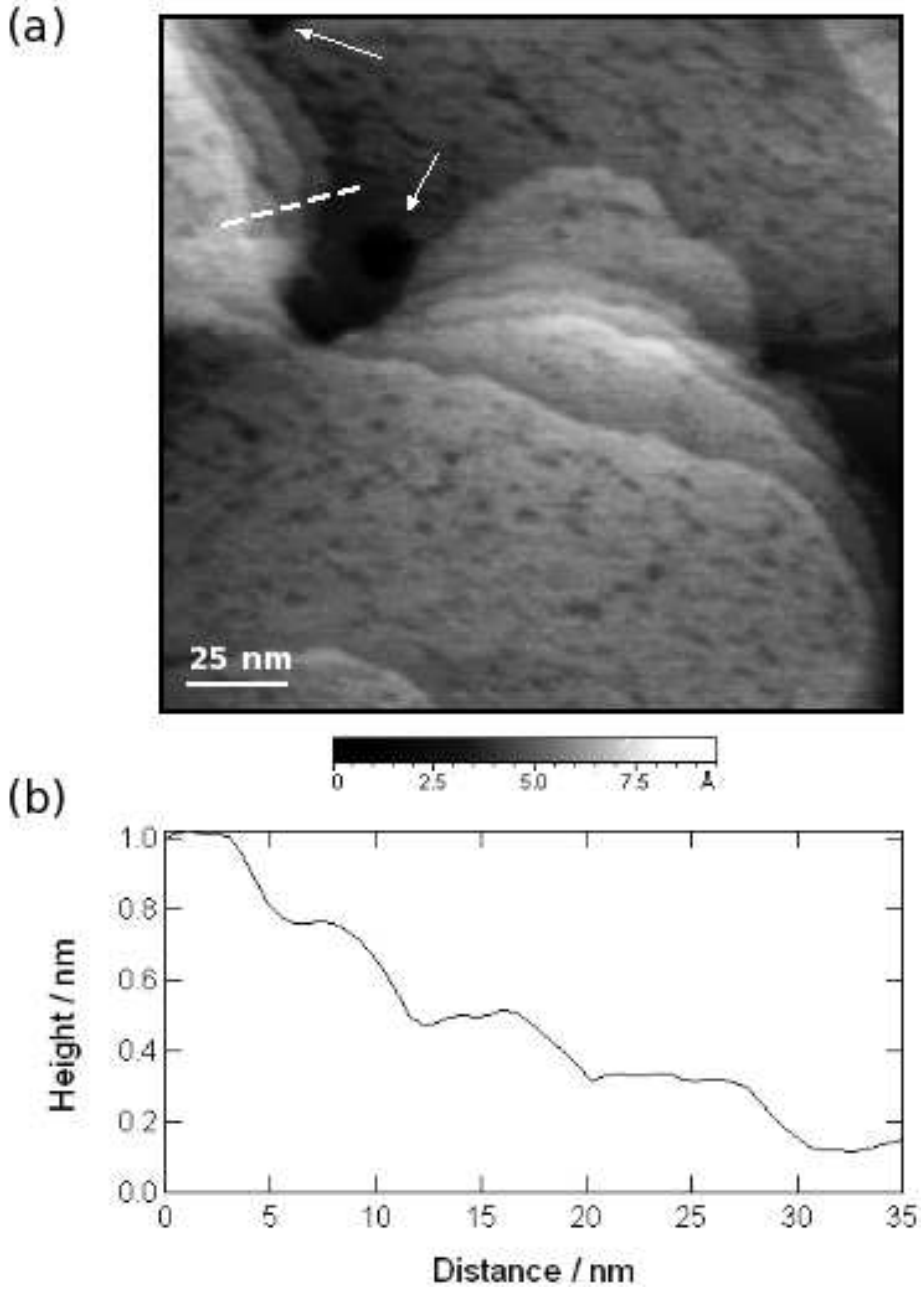

FIG. 2: (a) 200 nm × 200 nm high-resolution tapping mode AFM image of the Au:1 surface shown in height-mapped grayscale, featuring 0.25 nm high monatomic terraces and grain boundaries. The terrace edges are delineated by the {111} planes of the Au lattice. Examples of monatomic depressions in the Au surface are highlighted by arrows. (b) Height variation of successive monatomic Au step edges. This data represents the indicator line in the upper left of (a).

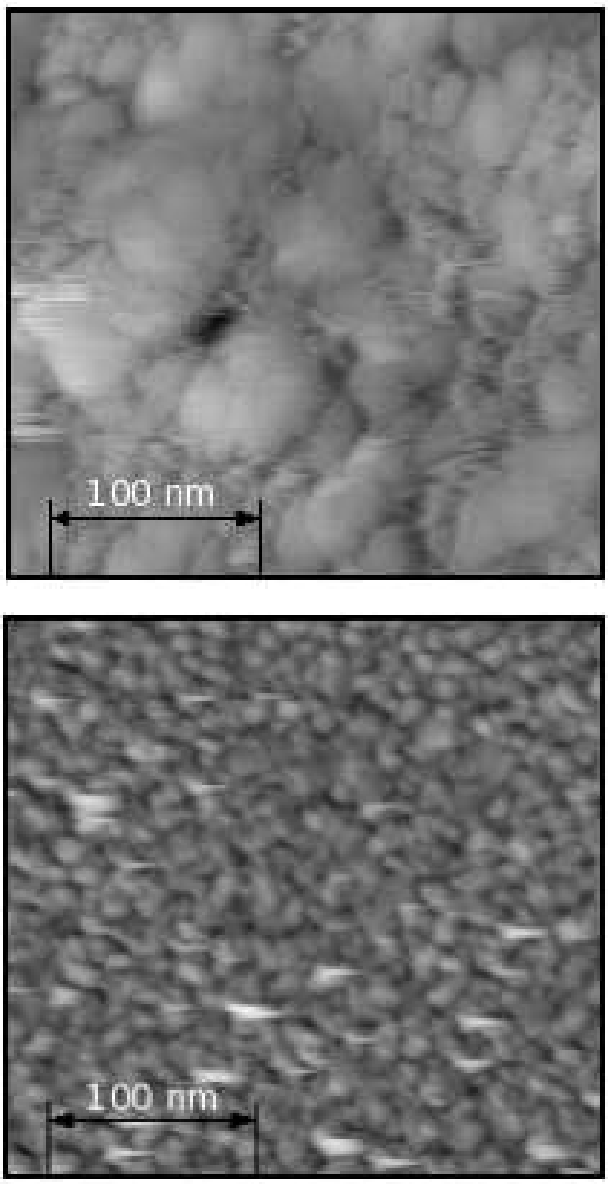

FIG. 3: (a) 300 nm × 300 nm STM image of the smoother Au:1 surface showing a lower density of grains. (b) 300 nm × 300 nm STM image of the Au:2 surface showing the high density of small grains. Both images were acquired under constant current conditions at a bias of +200 mV and a tunnelling current of 1 nA.

autocorrelation function to determine the grain size. Such an approach allows us to correlate the measured fractal dimension of the STM measurements to a fractal dimension which characterizes the roughness of the surface. The fractal dimension, D, of the film surfaces has been analyzed using a modified "slit island" technique [32]. This method is based on

the perimeter–area relationship developed by Mandlebrot [33, 34]. This relationship states that if an object with fractal dimension D is sliced, the perimeter and area of the resulting surface will fulfill the following relation

$$(\text{perimeter})^{\frac{1}{D-1}} = C \cdot (\text{area})^{\frac{1}{2}}$$

where $D-1$ is the fractal dimension of the slice and C is a constant. Different slices of the same object follow the same relation. Thus, in a graph of log(perimeter) versus log(area) for different slices, the slope of the corresponding line will be $(D-1)/2$. In the present case, the STM images are "sliced" by creating contour maps to which we apply this fractal analysis. The calculated fractal dimension, D, determined from the STM images of Fig. 3 give values of 2.02 and 2.26 for the Au:1 and Au:2 surfaces respectively. The overall surface topography of the Au:1 surface is relatively homogeneous, whereas for Au:2 surfaces, the grain structures responsible for the roughness are clearly visible. The obtained fractal dimension characterizes the influences of the granular structure on the roughness of the respective surface [32]. For Au:1 substares, the value of D approaches the value 2, indicating a smooth, nearly ideal 2-dimensional surface [32]. The grain structures align themselves parallel to the substrate orientation to produce a smoother surface.

From the STM topographies, an estimation of the grain size has been carried out using the autocorrelation function approach [35]. The autocorrelation function (acf), defined as

$$\text{acf}(\mathbf{a}) = \int i(\mathbf{r}) i(\mathbf{r}+\mathbf{a}) d\mathbf{r}$$

where $i(\mathbf{r})$ is the signal intensity or measured tunnelling current of a given STM scan and $i(\mathbf{r}+\mathbf{a})$ is the signal intensity $i(\mathbf{r})$ measured at a characteristic distance $|\mathbf{a}| = 1/N$, where N is the number of points in a particular scan. The net effect results in strong peak-like features, that correspond to correlated regions of the surface. The separation distance between these peaks reflect the average grain size distribution [32]. This procedure is repeated for each image of the same sample and the results are averaged. The grain sizes determined in this way from the STM data in Figs. 3a and 3b give values of 150 nm and 45 nm for the Au:1 and Au:2 surfaces respectively. Thus the larger grain size observed on the smoother Au:1 surface is advantageous for the adsorption of a relatively uniform nonanethiol monolayer, whereas the highly rough undulating granular surface morphology of the Au:2 substrates present a much more varied surface topography, unfavorable for controlled alkanethiol adsorption.

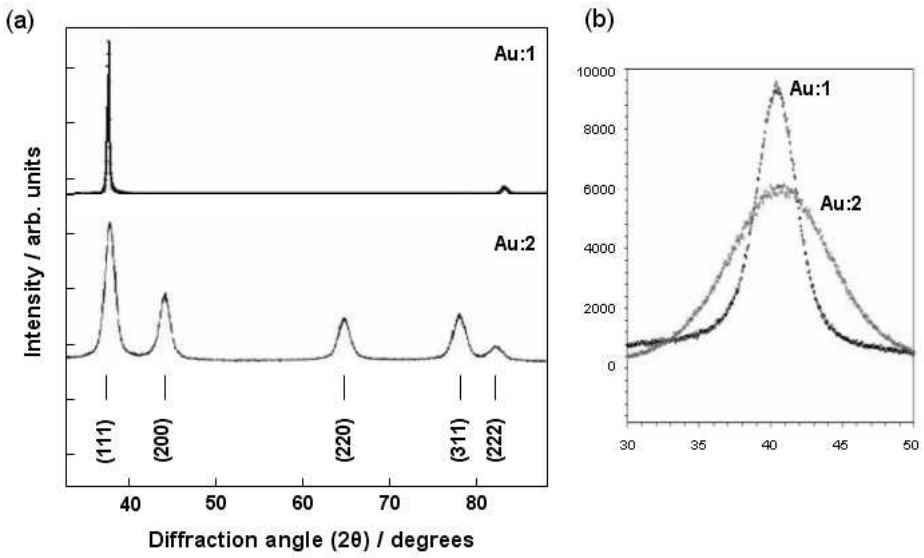

FIG. 4: (a) GIXRD spectra of the Au:1 and Au:2 layers. The spectra were acquired at grazing incidence to determine the preferential orientation of the grains without substrate contributions. On a logarithmic scale, no discernable peaks from {200}, {220} or {311} reflections of the Au lattice could be observed for the Au:1 surface. (b) High resolution normalized GIXRD spectra of the Au:1 and Au:2 layers for the {111} peak overlaid for comparison. The units are the same as those for (a).

2. Crystal orientation and grain density

Alkanethiol adsorption is dependent on the crystal orientation of the Au grains but the SAM monolayer *uniformity* is dependent on the density of grains with the same crystal orientation. We have employed grazing incidence X-ray diffraction (GIXRD) to characterize the crystal orientation of the grains in both the Au:1 and Au:2 surfaces and to quantify the relative density of each crystal orientation in both surfaces. The GIXRD spectra of the Au crystal structure is shown in Fig. 4a. For the Au:1 layer, two peaks were observed in the spectrum at 38.15° and 88.3°, which correspond to the {111} and {222} planes of the face-centered cubic structure of bulk Au, respectively. For the Au:2 layer, however, a number of peaks were observed at 38.15°, 44.35°, 64.6°, 77.9° and 83.8°, corresponding to the {111}, {200}, {220}, {311} and {222} planes. The inter-planar spacing of the sputtered Au layer, determined from the diffraction angle of the {111} plane in Fig. 4a, is measured to be 0.238 nm, in good agreement with that of the inter-planar spacing of bulk Au{111}

(0.24 nm). In both cases, the {111} peak shows the highest relative intensity indicating that a greater density of these grains exist in both types of surfaces. However, for the Au:1 surface only two crystal orientations are observed and the difference in relative intensity between these two peaks indicates that the surface is almost entirely composed of {111} oriented Au grains. In contrast Au:2 contains a number of crystal orientations; even though the energetically favorable {111} grain density is highest. As can be seen from the bottom panel of Fig. 4a, this density is just a fraction of that for the Au:1 surface.

In Fig. 4b, the normalized {111} reflections for both the Au:1 and Au:2 surfaces are overlayed. Individual fitting of the diffraction peaks was carried out by fitting the sample-dependent variables (angle position, intensity and line broadening) to the experimental diffraction profile using a Marquardt nonlinear least-squares algorithm [32]. It is observed that the Au:1 exhibits a higher relative intensity than the Au:2 surface by a factor of $\simeq$ 1.5. Furthermore, the {111} Bragg reflection from the Au:1 surface has a narrower line width indicating the degree of crystallinity in the Au:1 is greater than that of the Au:2 surface. This line width narrowing implies that the grain sizes for the Au:1 surface are greater than those on the Au:2 surface, in good agreement with the STM information. From Fig. 4a, the quantitative percentage of {111} terminated surface on Au:1 and Au:2 can be determined by fitting the rocking curves with a pseudo-Voigt function [36]. A value of 0.94 is determined for the fraction of the surface terminated with this crystal orientation. The fraction of the surface terminated with the {111} face for the Au:2 is determined to be 0.49, almost half that for the Au:1 surface, which agrees well with the higher intensity of the {111} peak in the GIXRD curves in Fig. 4b and the higher degree of {111} crystallinity of the Au:1 surface is consistent with the observed line width narrowing.

Thus, AFM, STM and GIXRD studies of the sputtered Au:1 and evaporated Au:2 surfaces, shows that sputtered Au surfaces exhibit a much lower degree of roughness, and sputtered Au surfaces contain a higher density of {111} oriented Au grains, a distinct advantage for the adsorption of alkanethiols [26, 31]. The physical properties for sputtered and evaporated Au surfaces are summarized in Table I. The 150 nm size of {111} grains on Au:1 surfaces is $\simeq$3 times greater than the SAM film thickness, and suggests single-crystal epitaxial growth. Some monatomic depressions exist on the surface of each grain prior to treatment in the alkanethiol solution, but we have recently demonstrated that the alkanethiol covers the surface and depressions alike [26, 31]. Thus sputtered Au films produce

good quality substrates for alkanethiol-based resist adsorption for atomic nanolithography applications.

C. Alkanethiol coverage and dependence on Au morphology

There have been numerous reports of substrate-induced effects on the quality of the patterns produced after etching in atomic nanolithography processes [25, 27]. However, all such reports have apportioned blame for poor quality on either the roughness of the substrate or on the grain size. While these parameters certainly do have an effect on the coverage by alkanethiols of Au surfaces, thus far no analysis of alkanethiol coverage of Au substrate *prior* to the etching step have been performed. We have employed both phase imaging non-contact AFM and lateral force contact AFM techniques to characterize the SAM/Au surface immediately prior to use in nanolithographic experiments. Although grain size and surface roughness contribute, our studies have revealed that the coverage uniformity depends first and foremost on the crystal orientation of the grains.

As discussed in Section III B, sputtered substrates give smoother surfaces than evaporated Au surfaces and show a much lower density of grains. More importantly, however, the Au:1 surface also contains a much greater proportionate density of {111} oriented Au grains. The fraction of the surface displaying the crystal faces corresponding to these reflections is important because at least one of them, the {100} face, is associated with an incommensurate arrangement of the monolayer lattice and correspondingly weaker SAM-Au bonding. There have been no reports of SAM adsorption on Au{200}, Au{311} or on Au{222}. Figures 5a and 5b show non-contact AFM images of the SAM on Au:1 and Au:2 surfaces respectively. Both topographical and phase imaging were acquired simultaneously. Phase imaging allows the determination of the variation in composition of a particular surface. In this case, the alkanethiol monolayer is shown in black and the Au surface is white/bright gray.

By numerical integration of monotone images such as the phase images in Figs. 5a and 5b, the percentage total coverage of the SAM was found to be 59% and 21% for Au:1 and Au:2 surfaces respectively. Note that the percentage coverage of the Au:1 surface by the SAM is 35% less than its percentage coverage by {111} terminated Au faces. The phase imaging information implies therefore that alkanethiol adsorption to other crystal orientations occurs.

Nevertheless atomically flat surfaces such as those found on Au:1 surfaces are conducive

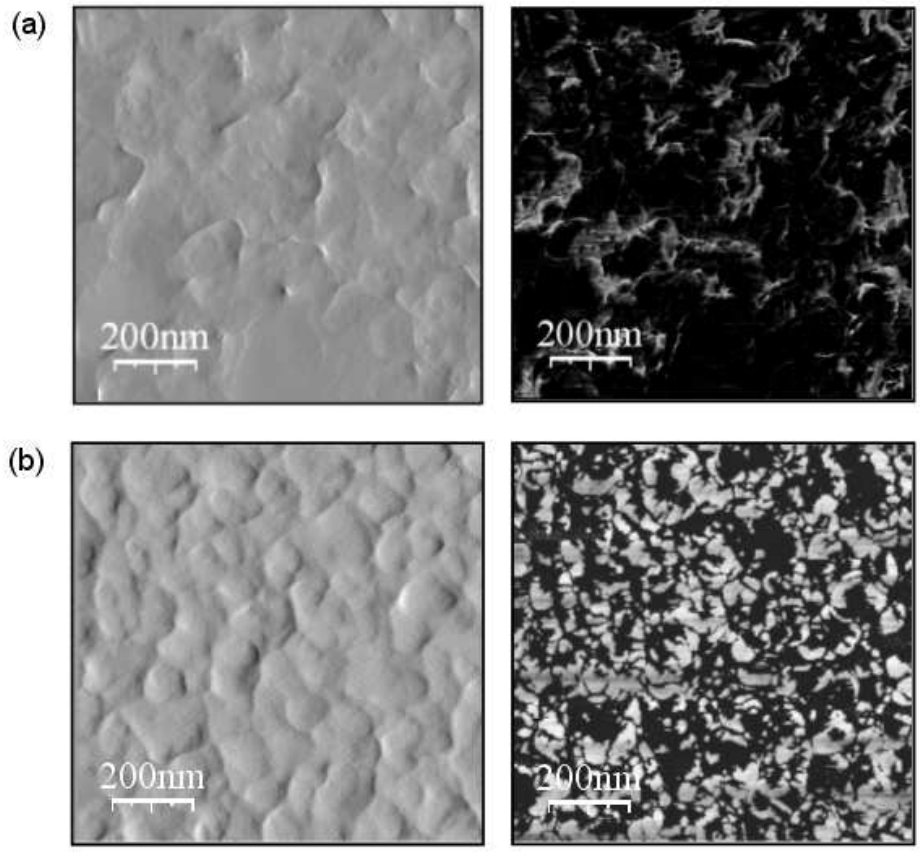

FIG. 5: (a) Tapping mode AFM image of the alkanethiol monolayer covered Au:1 surface (left panel), and its corresponding phase image (right panel). (b) Tapping mode AFM image (left panel) and corresponding phase image (right panel) for the Au:2 surface covered with the alkanethiol monolayer. Imaging of both samples was done under identical conditions (laboratory and AFM parameters).

to the growth of ordered SAMs. Figure 6a shows an STM image of the alkanethiol SAM on the sputtered Au surface. Such large scale STM surface survey images show the highly variable coverage of the Au by the SAM on Au monatomic terraces. The surface is observed to consist of a mosaic-like network of domains ranging in size from approximately 5-25 nm, with some defect-free domains observed to extend to more than 50 nm. It can also been observed that monolayer domains, highlighted in the image, are present over the full surface area of each terrace. More detailed analysis on the domain formation and characteristics can be found elsewhere [26]. A higher magnification STM image of the monolayer on Au:1 is shown in Fig. 6b. It can be observed that each domain consists of an ordered arrangement

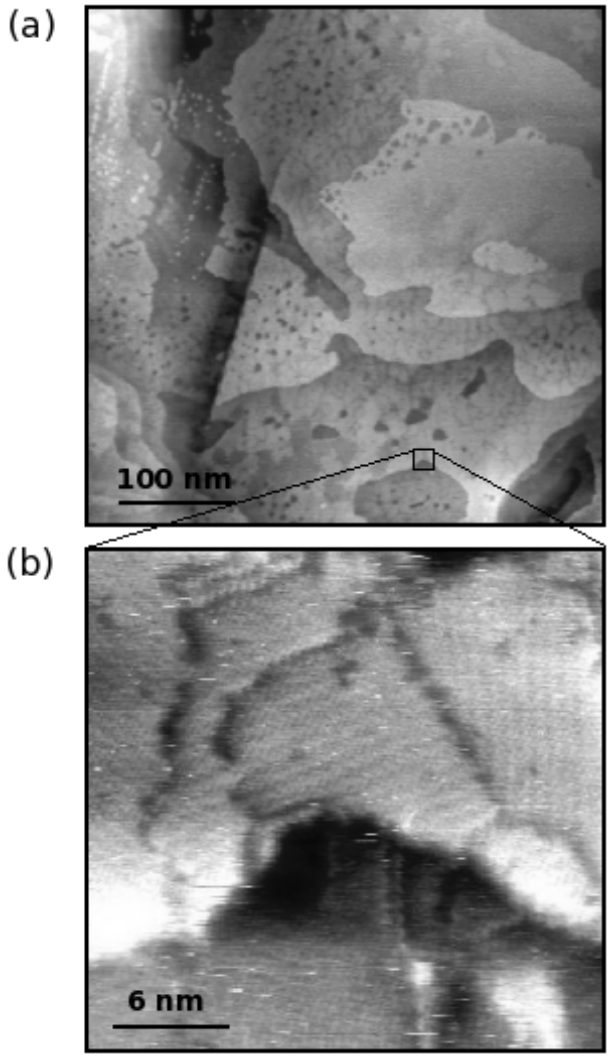

FIG. 6: (a) 425 nm × 425 nm STM image of the 1-nonanethiol on Au{111} terraces, where a large number of discontinuities such as domain boundaries, pinholes and monatomic depressions are observed. (b) Higher resolution 25 nm × 25 nm STM image of the area highlighted in (a) showing molecular scale domain boundaries and ordered alkanethiol molecule arrangement on Au{111} terraces.

of alkanethiol molecules. Indeed, the packing arrangement is identical and coherent within a single domain, *i.e.* all atoms are arranged such that the unit cell axes of the packing arrangement remain unchanged within the domain itself. Each of the domains are separated by domain boundaries typical of molecular scale dimensions. Such boundaries are identified in Fig. 6b as dark fissures between domains. Most boundaries are observed to have three orientations originating from the hexagonal Au{111} three-fold surface symmetry, due to the

TABLE I: Characteristics of the sputtered Au:1 and evaporated Au:2 substrates

	Grain size (nm)	Fraction {111} (%)	Roughness (nm)	Fractal dimension	SAM coverage (%)
Au:1	150	0.94	1.8 ± 0.4	2.02	59
Au:2	45	0.49	6.7 ± 1.2	2.26	21

remarkable degree of epitaxy that alkanethiol SAMs have with Au{111} surfaces. Even with exceptionally ordered sputtered Au surfaces composed of predominantly {111} terminated Au planes, the relative orientation of Au{111} grains also adds to the density of nonuniform features. Such boundaries limit the resolution of patterning achievable when SAMs are employed as positive resists in atomic nanolithography experiments. Table I summarizes the properties of Au:1 and Au:2.

D. Cs exposure of alkanethiol monolayer and optimization of feature resolution

Having characterized the influence of the Au surface on the coverage uniformity by the alkanethiol monolayer, we now turn to the exposure of this monolayer by a cold atomic Cs beam. Many groups report that alkanethiol resist-based nanolithography is not very reproducible [25, 52]. This lack of reproducibility is partially due to the quality of the Au substrate. However, for a complete lithographic process, the exposure of the alkanethiol with Cs atoms and the subsequent wet-etching steps are also critical stages in the eventual realization of the desired lithographic pattern. Various reports differ regarding the method of exposure of the alkanethiol molecules, the minimum Cs dose per molecule required to effect this exposure, the rate and anisotropy of the Au etching in suitable solutions. We have conducted detailed studies on all these issues to clarify the dependencies of all aspects of the nanolithographic process, and the results are presented in this section.

1. AFM/LFM studies of SAMs exposed to Cs flux

With an atomic beam of Cs (see Fig. 7 for a schematic diagram of the setup and Section III E 1 for details), transversely collimated and cooled by optical molasses [47, 48], we have exposed the alkanethiol resists through a material mask consisting of a woven wire mesh

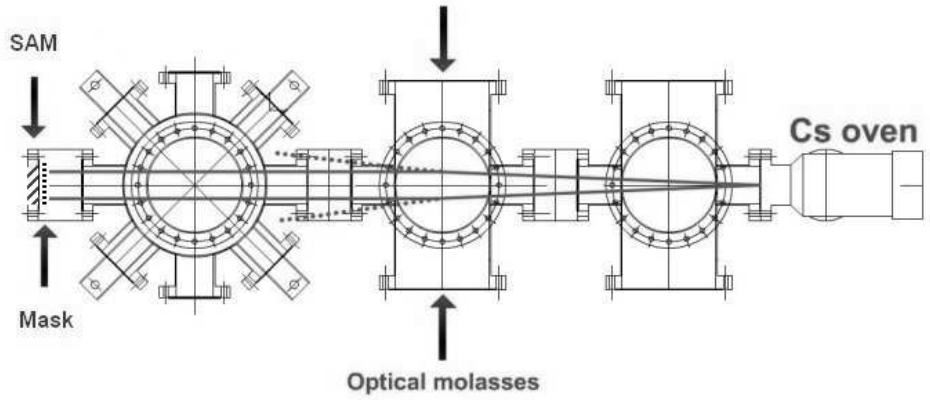

FIG. 7: Schematic diagram of the Cs atomic beam. The source is a thermal oven heated about 75 K above ambient temperature. An effusive beam issuing from the nozzle is collimated by transverse optical molasses that cools the transverse velocity components. The cross section of the beam is $\simeq$3 mm (see Fig. 10), and the residual divergence is less than 1 mrad. The Cs flux passes through the material mask and deposits on the SAM substrate.

(wire 30μm diameter, 80μm period). This relatively large periodic grid is easily imaged and thus amenable to systematic study. The alkanethiol coverage Au:1 substrate was exposed to the Cs beam for periods ranging from 5−30 mins at a flux density of $\simeq 10^{12}$ atoms cm^{-2} s^{-1}. After exposure the samples were immediately examined by AFM. Each AFM image was supplemented by lateral force microscopy (LFM) images of the surface taken simultaneously. LFM measures lateral deflections (twisting) of the cantilever that arise from forces on the cantilever parallel to the plane of the sample surface and thus is sensitive to the detection of differences in adhesion properties of the monolayer. Figures 8a and 8b show an AFM and corresponding LFM image of nonanethiol covered Au:1 substrates exposed to the Cs beam for 15 mins. It is observed that the topography measured by the AFM is a smooth surface, with little evidence of grid-like features identical to the material mask used in the exposure. In the adjoining LFM image, however, it can be clearly seen that the contrast shows a replica of the pattern, indicating that after 15 mins, the SAMs are sufficiently altered to be detected by LFM. These studies were also performed on samples exposed for 10 and 5 mins, but no features were observed with LFM in either case. The darker contrasting areas represent the Cs-exposed SAM and indicating that the torsional force experienced by the cantilever in contact with the exposed SAM is relatively less than that due to unexposed SAM. This observation indicates that the exposed SAM has a lower coefficient of friction

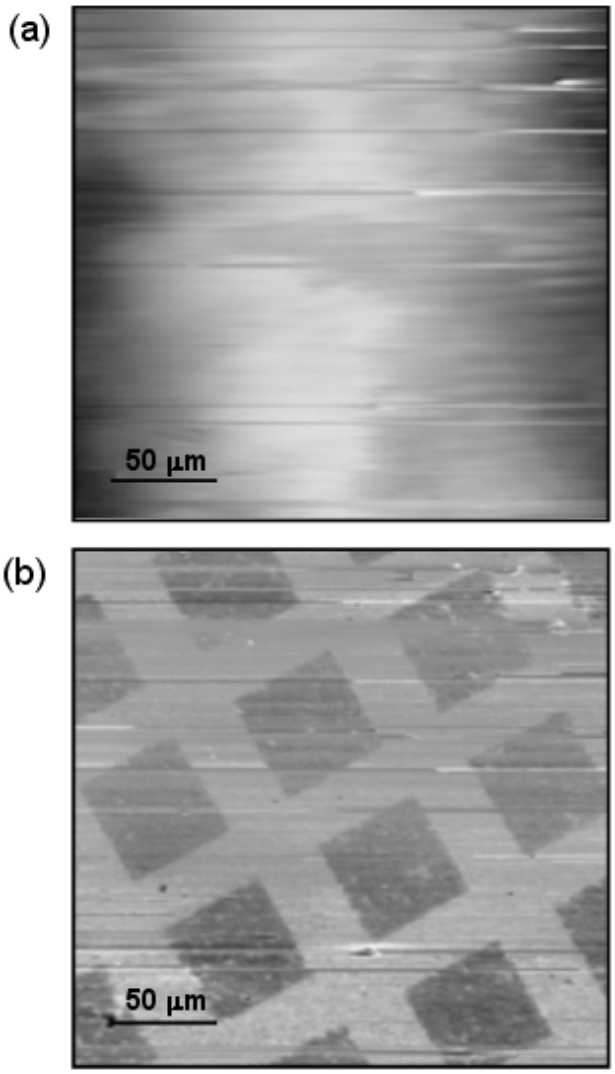

FIG. 8: (a) AFM image of the alkanethiol covered Au:1 surface after 15 mins exposure to the Cs beam showing a featureless topography. (b) LFM image of the same surface acquired simultaneously showing the replicated mask pattern caused by changes in the adhesion of the monolayer to the Au surface by exposure to the Cs beam. The LFM image shows that Cs patterning of the SAM can be measured even before the wet-etch development.

due to adhesion to the polar surface of the Si_3N_4 tip employed in the imaging.

2. Determination of the Cs flux minimum writing dose

In order to determine the minimum Cs dose, *i.e.* the number of Cs atoms required to render the SAM substrate susceptible to etching, the density of SAM molecules on the

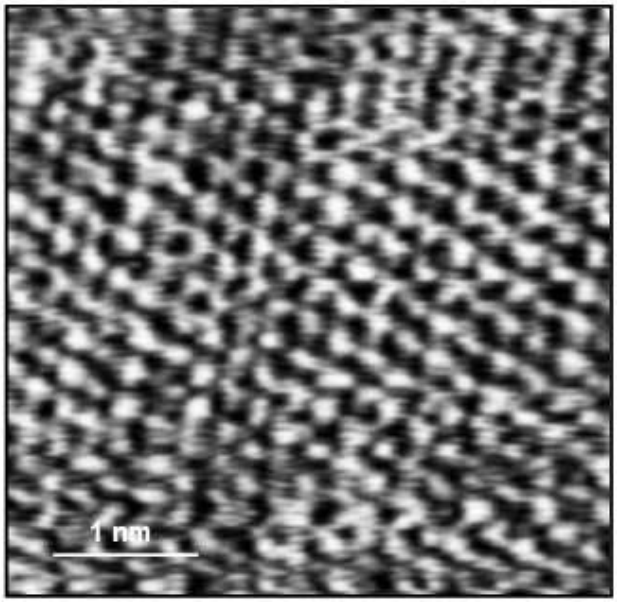

FIG. 9: Noncontact AFM image with molecular resolution of the alkanethiol covered Au:1 surface, showing the hexagonal packing arrangement of the molecular monolayer. The nearest-neighbor molecules are commensurate with the Au{111} lattice along the [112] directions.

surface of the Au has first to be determined. This measurement was acquired from high magnification and high resolution AFM images, such as that shown in Fig. 9, which is an atomic resolution AFM image of the alkanethiol covered Au:1 surface. From these high resolution AFM images, the hexagonal $(\sqrt{3} \times \sqrt{3})$R30° molecular arrangement [26, 31] can clearly be observed. From Fig. 9 an estimate for the density of alkanethiol molecules on Au{111} is $\simeq 4$ molecules nm^{-2}. This value is in agreement with previous reports [37–39] and gives an estimate for the molecular occupational density of $\simeq 4\times10^{14}$ cm^{-2}, assuming perfect hexagonal arrangement and no defects. Defects that appear as etch pits within the SAM monolayer can be ignored [26, 31]. Only the domain boundaries can affect the density calculation but a typical domain boundary is of the order of 2-4 lattice spacings. Thus, employing a Cs atomic beam with a flux of 10^{12} atoms cm^{-2} s^{-1}, 2.5×10^{-4} Cs atoms s^{-1} impinge on the surface per SAM molecule or a deposition rate of 0.15 monolayers min^{-1}. In order to determine the minimum number of Cs atoms needed to write a SAM monolayer, the Au/SAM surface was exposed to the Cs beam for times of 15 and 30 mins and then etched fully to remove all the underlying gold. Using the woven wire mesh mentioned previously, two samples were exposed to the entire cross sectional flux of the Cs beam, and AFM images

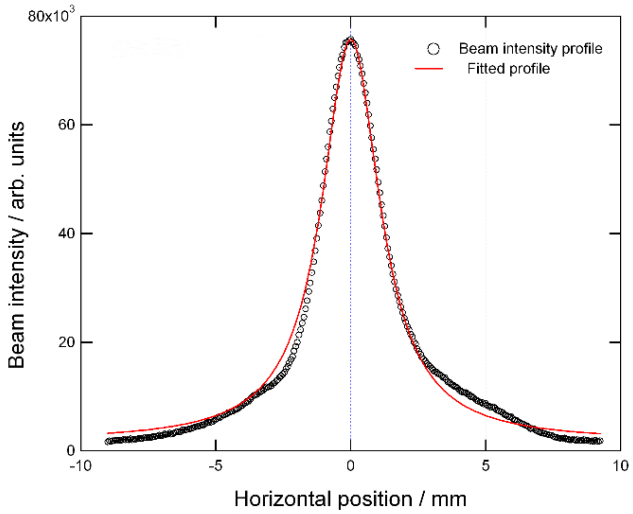

FIG. 10: The cross-sectional Cs beam intensity profile measured by a CCD camera fluorescence image of the 2D collimated Cs atomic beam during exposure of the alkanethiol monolayer.

(post-etch) were acquired to determine the number of written mask features. This procedure allows us to determine the dose that each part of the sample surface received. The feature dimensions were acquired from AFM images of the same surface so that the number of etched mask features written into the Au could be counted and converted to a real distance. Once acquired, the AFM feature dimensions were compared to the beam intensity profile, shown in Fig. 10, and converted to a corresponding flux. The Cs dosage at any position on the surface could be estimated since the Cs atomic beam profile (FWHM $\simeq 3$ mm) is well characterized by spatial atomic fluorescence distribution and a CCD camera. The furthest observable etch feature from the position on the surface corresponding to the centre of the Cs beam was observed at a distance of 1.26 mm. Thus, utilizing the beam profile in Fig. 10, the minimum Cs dose was estimated to be $\simeq 7.5\times10^{14}$ atoms cm^{-2}, which represents a minimum of $\simeq 2$ Cs atoms per SAM molecule. Therefore $\simeq 2$ monolayers of Cs are required to sufficiently alter the SAM to render it susceptible to wet etching. This dosage translates into a minimum exposition time of $\simeq 13$ min and is in good agreement with the LFM studies of the Cs exposed alkanethiol monolayer discussed earlier in this section.

3. Chemistry of the etch process

Having determined the Cs dose necessary to write an alkanethiol monolayer resist, optimization of the etching process is necessary to realize nano-scale lithographic patterns. The etching process requires a detailed study of the chemistry of the etching mechanism and etching nucleation processes of Au in ferricyanide solutions. When clean gold is exposed to an aqueous solution of cyanide ions in the presence of a mild oxidant, which in this case is the ferro/ferricyanide complex, the gold dissolves [40, 41]. The free energy of this process is dominated by the formation of the very stable and soluble $Au(CN)_2^-$ ion according to:

$$Au + 2CN^- + Fe(CN)_6^{3-} \rightarrow Fe(CN)_6^{4-} + Au(CN)_2^-$$

All of the etching experiments were conducted using SAMs formed from 1-nonanethiol, $HS(CH_2)_8CH_3$, although it has been reported that alkanethiols having longer chains provide comparable protection against etching. Shorter chain alkanethiols provide some degree of protection, but their ability to resist etching decreases with the length of the chain. For a cyanide based etchant, the absorption of CN^- ions on metals, in particular Au, can decrease their oxidation potentials by up to 2 V [42, 43]. Furthermore, the oxidation potential of Au can also be reduced by the chemisorption of sulfur-based compounds such as alkanethiols, but the magnitude of this reduction is much less than that for the CN^- ion [42, 43]. Adsorption of CN^- to the Au surface is prevented if the Au surface is covered with an alkanethiol molecule such as 1-nonanethiol used in this work. Thus the protected regions dissolve at a much slower rate than the exposed areas.

For etching solutions based on the cyanide ion, there are two principal properties necessary for an effective, selective etching solution. The solution must not contain a coordinating ion that can disrupt, damage or remove the adsorbed alkanethiol monolayer, and it should contribute toward the reduction in the oxidation potential of the Au by adsorption to the surface. This solution must also include an oxidant that oxidizes the Au in the presence of the coordinating ion with relative ease and have little or no effect on the alkanethiol monolayer. Thus the SAM must be impermeable and the efficient oxidation of the Au must occur. Ferricyanide, is such an efficient oxidant. The necessary step involving the reduction of the oxidation potential of the Au is maintained by using ferricyanide in a thiosulphate solution. Thiosulphate has an effect similar to cyanide in that it can reduce the Au oxidation potential, although the decrease is not as large as observed with CN^- ions. In the electrolyte

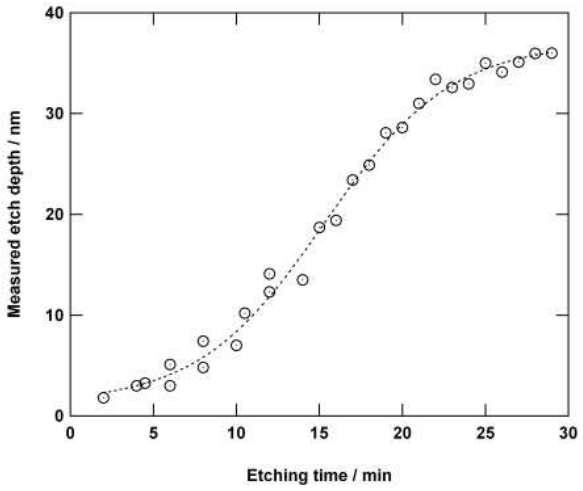

FIG. 11: Variation of the measured etch depth with etching time. All samples were etched under identical conditions and the AFM depth measurements were performed immediately after the etching step.

used in this work the ferricyanide oxidant, at a high concentration of 0.01 mol dm^{-3}, etches selectively; comparable to CN^- based etchants [43].

Numerous Au:1 samples were etched for various lengths of time in order to determine the actual etch rate. Each etching process was carried out under identical conditions and the resulting variation in height between the etched and unetched parts of the surface was measured using AFM.

Figure 11 shows the variation of the etch depth with time. A maximum effective etch rate of 2.2 nm min^{-1} was measured. Dissolution of the Au commences at a lower rate, where the nucleation of the etching occurs and thus an effectively smaller cumulative area of Au is being etched. Details on the nucleation mechanism of the Au etching will be published elsewhere [44, 45]. Complete etching of the Au occurs after 25-30 mins, where the rate reduces to zero.

In order to optimize this etch development, we observed the process *in-situ* and in real time. The same woven wired mesh discussed in the phase imaging of Fig. 8 was again used to write a Cs periodic pattern on the SAM surface. During the wet-etch process a HeNe laser illuminated the developing periodic pattern directly through the etching solution. The resulting diffraction pattern was recorded on a CCD camera and the first-order diffraction intensity is shown in Fig. 12.

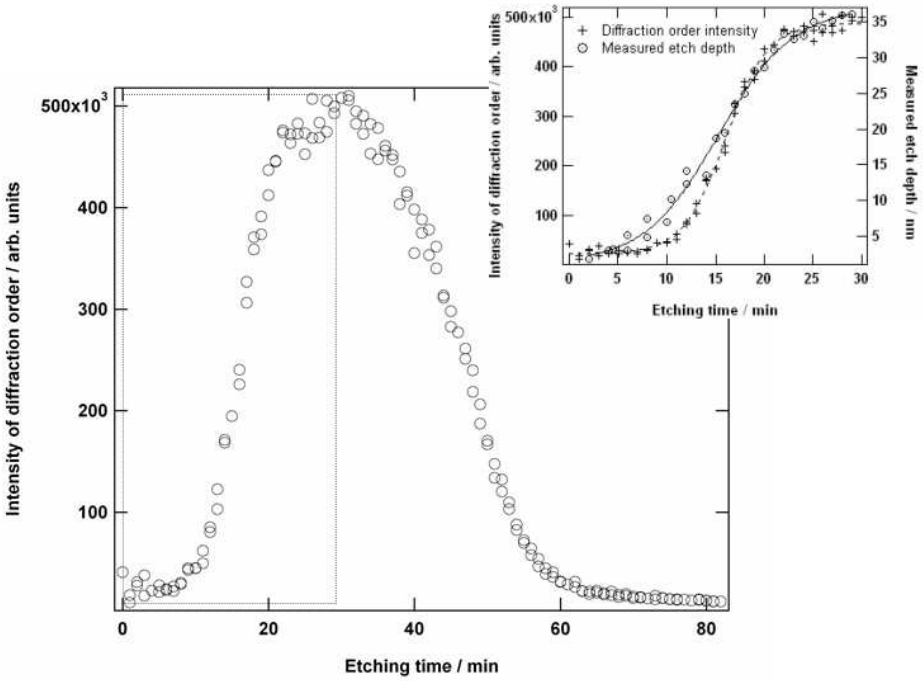

FIG. 12: Variation of the first order diffraction spot intensity reflected from the Au surface with etching time. The intensity was measured using a CCD camera while the sample remained in the etching solution. A 5 mW He-Ne laser was used for incident radiation. (*inset*) Overlay of data from Figs. 11 and 12 showing the correlation between etch rate and measured *in-situ* diffraction intensity.

The diffraction intensity is a direct measure of the definition of the periodic structures on the surface, and thus the measured intensity is proportional to the etch rate of the gold. The spatial and temporal characteristics of the diffraction pattern reveal certain properties of the etch process. We note that at any given time during the development, the intensity of the diffraction orders fall off smoothly, the first order intensity always dominant. This smooth intensity drop-off with order implies that the periodic structure is spatially uniform and continues to develop in time without the disordered appearance of spatially separated nucleation sites. As shown in Fig. 12, the best pattern definition is observed after etching for 25-30 mins. In the inset to Fig. 12, the data from Fig. 11 is overlaid with the data from Fig. 12, and it can be observed that there is strong correlation between the diffraction intensity and the etch rate of the Au:1 surface. It is interesting to note that both curves have the same overall shape with the maximum slope in both cases being at 50% of maximum. Furthermore, after 17 mins the data overlap, implying that the measured

intensity is directly proportional to the amount of Au etched. A similar trend in diffraction intensity and dissolved thickness of bare gold was found by Kumar *et al.* [46].

Thus a minimum dose of 2 monolayers of Cs, or 2 Cs atoms per nonanethiol molecule, is necessary to write the SAM. Systematic measurements of the etching of the exposed SAM indicate that an etching time of 25-30 mins allows for complete etching of the Au under exposed areas and the best feature definition. The studies show that for very small feature sizes that are in close proximity, merging of features can occur if the etching time is too long. As shown in Fig. 12, the diffraction intensity decreases after about 30 mins indicating that the periodic pattern definition begins to reduce after that time.

E. Patterning SAM resist using submicron apertures

By employing the optimizations discussed in Section III D for Cs beam exposure of the alkanethiol layer and the etching process, we have been successful in writing submicron features using material masks. The following is a brief description of the atomic beam used in these experiments.

1. Cs atomic beam

Figure 7 shows a schematic diagram of the thermal Cs beam used to expose the material masks. A thermal oven source heats a Cs metal reservoir to 373 K; and the Cs atomic beam effuses through an output nozzle, a long narrow tube 36 mm in length, 1.6 mm diameter. Optical molasses [47] cools the transverse velocity components of the beam, resulting in a "bright" [48] Cs atom beam, highly collimated to a divergence <1 mrad along the z direction. The beam has an average forward velocity of 150 m s^{-1}, a forward flux density of $\simeq 10^{12}$ atoms cm^{-2} s^{-1} and a residual divergence of ≤ 1 mrad.

2. Material masks

The submicron structures were designed for use with a concentrated atomic beam [38] and consist of 2-D arrays of a submicron aperture at the point of a hollow pyramidal tip. The base of each pyramid in the array measures $\simeq 22\mu$m on a side, and the pyramids are

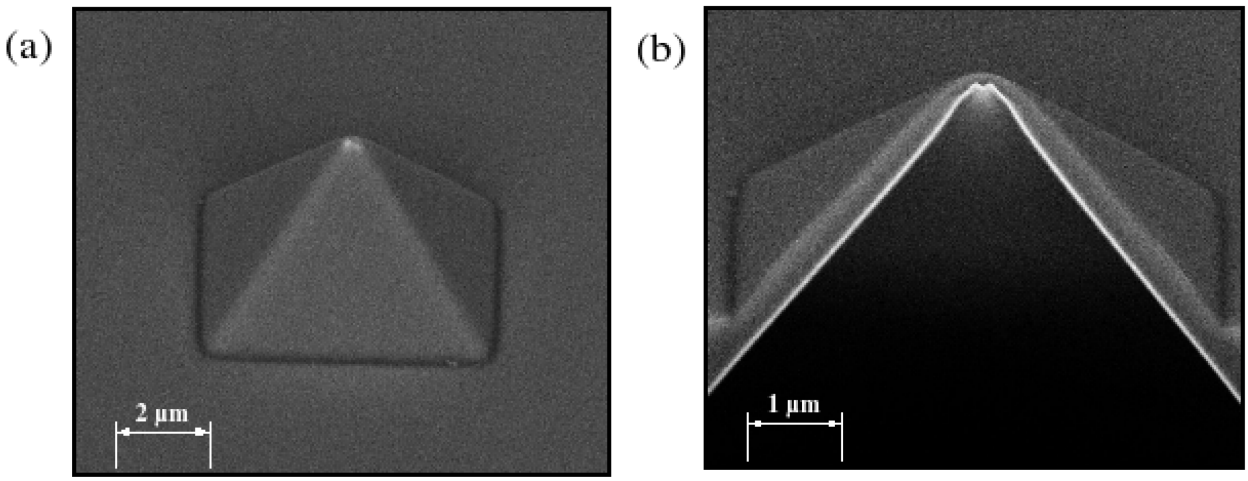

FIG. 13: (a) A secondary electron image of the pyramidal tips used in the nanolithography experiments. The left panel shows one of the pyramidal structures with a 200 nm hole in the apex of the tip. The base of the pyramid, as shown after the wet-etch process, is 3.5 μm on a side. The overall base of the pyramidal structure is 22 μm on a side. (b) The right panel shows a FIB milled cross-section of a pyramidal aperture.

separated by 3μm. The aperture array periodicity is therefore 25μm. Aperture formation is based on two self-adjusting parallel processes [49]. In the first process tetrahedral pyramids are formed in (001) oriented p-doped, 3-inch silicon wafers by well-known anisotropic wet etching in aqueous KOH solution at temperatures $\simeq 300\,\mathrm{K}$. This process is followed by steam oxidation at temperatures $\simeq$ 1273 K to form a 200 nm thin silicon dioxide layer. Applying reactive ion etching (RIE) with CHF_3 allows to selectively open the oxide at the apex of the pyramidal etch pits. After piercing the silicon dioxide layer in this way the underlying silicon substrate is partly removed to free the hollow silicon dioxide tips each carrying an aperture of around 100-400 nm depending on process parameters [50]. Scanning electron microscopy (SEM) images of one pyramidal structure is shown in Fig. 13. The aperture diameter used during experiments varied typically from 300 nm to 150 nm in diameter and was located 15 μm above the SAM surface (*i.e.* the pyramidal base was in contact with the SAM and each pyramid has a height of 15 μm from base to tip).

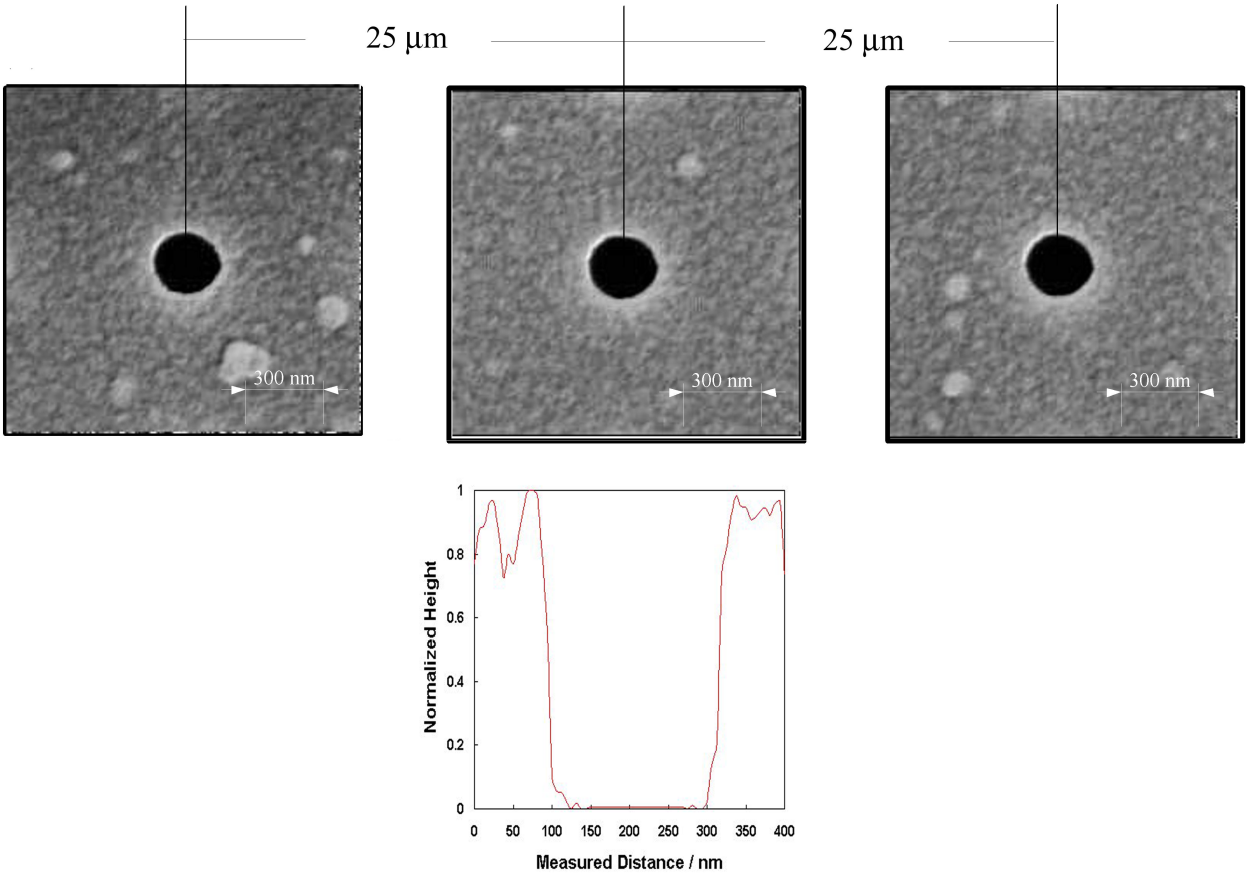

FIG. 14: Top panel: AFM images of a nonanethiol SAM written by a 15 minute Cs beam exposure through an array of pyramidal masks similar to the one shown in Fig. 13. The aperture in the point of the pyramid was 300 nm and the pyramid array was oriented with the points facing "upstream" toward the Cs flux. The height of the aperture above the SAM surface $\simeq 16\mu$m. The diameter of the written holes after the standard etch procedure was measured to be 280 nm. Bottom panel: Measured profile of one of the etched holes after the 15 minute exposure and etch treatment. The steep sides on the etched hole indicate the high resolution and sharp contrast achievable with this technique. The fractional depth gradient on the side wall is measured to be 0.8/20 nm

3. AFM images of written SAMs

Figure 14 shows AFM images and a line profile for SAMs exposed for 15 mins through the 2-D array of pyramidal masks then developed according to the procedures outlined in Section III D. In this particular mask the aperture in the pyramidal point was 300 nm.

IV. CONCLUSIONS

We have presented a detailed study of alkanethiol monolayer properties as a function of Au substrates for atomic nanolithography process optimization. We have found the coverage dependency, post-etch pattern definition and submicron features size to be influenced primarily by the quality and morphology of the Au substrate. Sputtered Au substrates yield smoother surface with a higher density of {111} oriented grains than evaporated Au surfaces. Phase imaging with AFM shows that that the quality and percentage coverage of uniform alkanethiol monolayer self-assembly is much greater for sputtered Au substrates. Exposure of the monolayer resist with a collimated atomic Cs beam allowed the determination of the minimum Cs dose required to alter the Au-S bonding thus exposing the resist. Employing lateral force microscopy, the minimum Cs dose was measured to be 2 Cs atoms per alkanethiol molecule or 2 monolayers of Cs deposited on the SAM surface. Systematic studies of a suitable wet-etching process in a water based cyanide etchant yielded an etch rate of $\simeq 2.2$ nm min^{-1} allowing optimization of patterned feature resolution. Utilizing these results, submicron features as small as $\simeq 230$ nm were etched into the Au layers using pyramidal aperture masks. The data presented are important for the continued application of atomic nanolithography to the realization of massively parallel writing of arbitrary structures currently under investigation [55].

[1] G. L. Timp, R. L. Behringer, D. M. Tennant, J. E. Cunningham, M. Prentiss, K. K. Berggren, Phys. Rev. Lett. **69**, 1636 (1992).

[2] M. Prentiss, G. Timp, N. Bigelow, R. E. Behringer, J. E. Cunningham, Appl. Phys. Lett. **60**, 1027 (1992).

[3] R. J. Celotta, R. Gupta, R. E. Scholten, J. J. McClelland, J. Appl. Phys. **79**, 6079 (1996).

[4] H. Metcalf, P. van der Straten, Phys. Rep. **244**, 203 (1994).

[5] C. S. Adams, M. Sigel, J. Mlynek, Phys. Rep. **240**, 143 (1994).

[6] R. Lüthi, R. R. Schlittler, J. Brugger, P. Vettiger, M. E. Welland, and J. K. Gimzewski, Appl. Phys. Lett. **75**, 1314 (1999).

[7] J. H. Thywissen, K. S. Johnson, R. Younkin, N. H. Dekker, K. K. Berggren, A. P. Chu, M. Prentiss, S. A. Lee, J. Vac. Sci. Technol. B **15**, 2093 (1997).

[8] M. J. Lercel, H. G. Craighead, A. N. Parikh, K. Seshadri, D. L. Allara, Appl. Phys. Lett. **68**, 1504 (1996).

[9] K. K. Berggren, A. Bard, J. L. Wilbur, J. D. Gillaspy, A. G. Helg, J. J. McClelland, S. L. Rolston, W. D. Phillips, M. Prentiss, G. M. Whitesides, Science **269**, 1255 (1995).

[10] S. V. Atre, B. Lieberg, D. L. Allara, Langmuir **11**, 3882 and references therein (1995).

[11] L. H. Dubois, R. G. Nuzzo, Annu. Rev. Phys. Chem. **43**, 437 (1992).

[12] J. F. Ford, T. J. Vickers, C. K. Mann, J. B. Schlenoff, Langmuir **12**, 1944 (1996).

[13] O. Chailapakul, L. Sun, C. Xu, R. M. Crooks, J. Am. Chem. Soc. **115**, 12459 (1993).

[14] P. A. DiMilla, J. P. Folkers, H. A. Biebuyck, R. Haerter, G. P. Lopez, G. M. Whitesides, J. Am. Chem. Soc. **116**, 2225 (1994).

[15] L. H. Dubois, B. R. Zegarski, R. G. Nuzzo, J. Chem. Phys. **98**, 678 (1993).

[16] M. M. Walczak, C. A. Alves, B. D. Lamp, M. D. Porter, J. Electroanal. Chem. **396**, 103 (1995).

[17] R. C. Tiberio, H. G. Craighead, M. Lercel, T. Lau, C. W. Sheen, D. L. Allara, Appl. Phys. Lett. **62**, 476 (1993).

[18] L. Salem, J. Chem. Phys. **37**, 2100 (1962).

[19] D. J. Lavrich, S. M. Wetterer, S. L. Bernasek, G. Scoles, J. Phys. Chem. **102**, 3456 (1998).

[20] S. Sun, G. J. Leggett, Nano Lett. **2**, 1223 (2002).

[21] S. Sun, K. S. L. Chong, G. J. Leggett, J. Am. Chem. Soc. **124**, 2414 (2002).

[22] Y. Xia, G. M. Whitesides, Annu. Rev. Mater. Sci. **28**, 153 (1998).

[23] Y. Xia, X. M. Zhao, G. M. Whitesides, Micro. Eng. **32**, 255 (1996).

[24] J. L. Wilbur, A. Kumar, H. A. Biebuyck, E. Kim, G. M. Whitesides, Nanotechnology **7**, 452 (1996).

[25] J. C. Love, D. B. Wolfe, M. L. Chabinyc, K. E. Paul G. M. Whitesides, J. Am. Chem. Soc. **124**, 1576 (2002).

[26] C. O'Dwyer, G. Gay, B. Viaris de Lesegno, J. Weiner, Langmuir **20**, 8172 (2004).

[27] M. T. Lee, C. C. Hsueh, M. S. Freund, G. S. Ferguson, Langmuir **14**, 6419 (1998).

[28] B. D. Cullit, *Elements of X-ray Diffraction*, Addison-Wesley, Reading 1978.

[29] E. Delamarche, B. Michel, C. Gerber, D. Anselmetti, H.-J. Guntherodt, H. Wolf, H. Ringsdorf, Langmuir **10**, 2869 (1994).

[30] H. Berger, Krist. Tech. **11**, 1171 (1976).

[31] G. E. Poirier, M. J. Tarlov, Langmuir **10**, 2853 (1994).

[32] J. Nogués, J. L. Costa, K. V. Rao, Physica A **182**, 532 (1992).

[33] B. B. Mandelbrot, *The Fractal Geometry of Nature*, Freeman, San Francisco (1982).

[34] B. B. Mandelbrot, D. E. Passoja, A. J. Paullay, Nature **308**, 721 (1984).

[35] G. Reiss, H. Brückl, J. Vancea, R. Lecheeler, E. Hastreiter, J. Appl. Phys. **70**, 523 (1991).

[36] R. A. Young, D. B. Willes, J. Appl. Cryst **15**, 430 (1982).

[37] T. Ohgi, H. Y. Sheng, Z. C. Dong, H. Nejoh, Surf. Sci. **442**, 277 (1999).

[38] M. Kreis, F. Lison, D. Haubrich, D. Meschede, S. Nowak, T. Pfau, J. Mlynek, Appl. Phys. B. **63**, 649 (1996).

[39] J. Li, K. S. Liang, N. Camillone III, T. Y. B. Leung, G. Scoles, J. Chem. Phys. **102**, 5012 (1995).

[40] A. M. Brittan, Am. Sci. **62**, 402 (1974).

[41] F. A. Cotton, G. Wilkinson, Advanced Inorganic Chemistry 4th ed., 966 Wiley, New York (1980).

[42] R. J. Puddephatt, The Chemistry of Gold, Elsevier, Amsterdam (1978).

[43] R. L. McCarley, Y. T. Kim, A. J. Bard, J. Phys. Chem. **97**, 211 (1993).

[44] C. O'Dwyer, (unpublished).

[45] C. O'Dwyer, (unpublished).

[46] A. Kumar, H. A. Biebuyck, G. M. Whitesides, Langmuir **10**, 1498 (1994).

[47] An introduction to the physics of optical cooling and trapping can be found in two special issues of the Journal of the Optical Society of America B. These are: J. Opt. Soc. Am. B **6**, No. 11 (1985) and J. Opt. Soc. Am. B **6** No. 11 (1989).

[48] W. DeGraffenreid, Y.-M. Liu, J. Ramirez-Serrano, J. Weiner, Rev. Sci. Instr. **70**, 3668 (2000).

[49] A. Vollkopf, O. Rudow, E. Oesterschulze, J. Electrochem. Soc. **148**, G587 (2001).

[50] G. Georgiev, M. Müller-Wiegand, A. Georgieva, K. Ludolph, E. Oesterschulze, J. Vac. Sci. Technol. B **21**, 1361 (2003).

[51] A. Camposeo, A. Piombini, F. Cervelli, F.Tantussi, F. Fuso, E. Arimondo, Opt. Comm. **200**, 231 (2001).

[52] A. Camposeo, F. Cervelli, A. Piombini, F. Tantussi, F. Fuso, M. Allegrini, E. Arimondo, Mat. Sci. Eng. C **23**, 217 (2003).

[53] H. J. Metcalf, P. van der Straten, Laser Cooling and Trapping, Springer, New York (1999).

[54] J. J. McClelland, R. E. Scholten, E. C. Palm, R. J. Celotta, Science **20**, 2535 (1995).

[55] M. Mützel, M. Müller, D. Haubrich, U. Rasbach, D. Meschede, C. O'Dwyer, G. Gay, B. Viaris de Lesegno, J. Weiner, K. Ludolph, G. Georgiev, E. Oesterschulze, (unpublished).